Energy Storage Materials 84 (2026) 104862

Contents lists available at ScienceDirect

Energy Storage Materials

journal homepage: www.elsevier.com/locate/ensm

Amino acid-based complexing agents for improved Zn anode performance in near-neutral aqueous Zn-air batteries

Eunmi Im [a], Rebecca Erkes [a], Marie Heidler [a], Jinhong Mun [b], Saul Said Montiel Guerrero [a], Jee Ho Ha [c], Krzysztof Dzieciol [a], Shicheng Yu [a], Hans Kungl [a], Hermann Tempel [a], Geunsik Lee [b], Yasin Emre Durmus [a,*], Rüdiger-A. Eichel [a,d]

[a] Institute of Energy Technologies-Fundamental Electrochemistry (IET-1), Forschungszentrum Jülich, 52428, Germany
[b] Department of Chemistry, School of Natural Science, Ulsan National Institute of Science and Technology (UNIST), Ulsan 44919, South Korea
[c] Department of Energy Engineering, School of Energy and Chemical Engineering, Ulsan National Institute of Science and Technology (UNIST), Ulsan 44919, South Korea
[d] RWTH Aachen University, Institute of Physical Chemistry, Aachen 52074, Germany

ARTICLE INFO

Keywords:
Zinc-air battery
Aqueous electrolyte
Electrolyte additive
Complexing agents

ABSTRACT

Aqueous electrolytes used in zinc–air batteries often face issues with low stability and unwanted side reactions, especially under alkaline conditions. This highlights the need for alternative electrolyte systems, such as near-neutral electrolytes. In this study, we explore the innovative use of amino-acid–based complexing agents, specifically glycine (Gly) and iminoacetic acid (IDA), to enhance the performance of Zn electrodes in a 2 M NaCl electrolyte. Unlike traditional additives, these amino acids serve a multi purpose: they coordinate with Zn^{2+} ions in the bulk electrolyte and simultaneously regulate the interface between Zn and the electrolyte, while providing pH stability. Density functional theory (DFT) calculations indicate that this unique interaction alters the solvation shell of Zn^{2+}, which helps reduce the formation of a passivation layer. In-operando X-ray computed tomography (XCT) further demonstrates that the amino-acid additives facilitate uniform Zn deposition and improve the cycling stability of the plating and stripping process. This work highlights the significance of solvation shell modulation in optimizing electrochemical performance and offers valuable insights for the development of near-neutral electrolyte-based Zn-air batteries.

1. Introduction

The growing demand for renewable energy brings attention to the urgent need for reliable grid-scale energy storage solutions. However, renewable energy sources such as wind and solar are inherently fluctuating and geographically dependent, resulting in an unstable power supply. This challenge has accelerated the development of the next generation energy storage system [1].

Among the various promising candidates [2], rechargeable zinc-air batteries (ZABs) have received much attention because of their high theoretical specific energy (1,086 Wh kg^{-1}) utilizing cost-effective Zn metal [3,4]. In addition, ZABs use oxygen from the surrounding air as a reactant at the cathode and employ aqueous electrolytes. This design offers several benefits, including reduced system weight, lower costs, and enhanced safety [4–6]. However, despite these advantages, the practical performance of ZABs is still limited by several challenges. These include dendrite formation, hydrogen evolution reaction (HER), corrosion, surface passivation, and carbonization of the electrolyte, all of which can degrade electrochemical performance across a wide pH range [7–10].

Alkaline electrolytes are widely used in ZABs because they exhibit high ionic conductivity and are cost effective. These electrolytes facilitate the formation of zinc oxide species (e.g., ZnO, $Zn(OH)_2$, $Zn(OH)_3^-$), influencing the formation of the passivation layer and accelerating dendrite growth, which can ultimately restrict the lifespan and rechargeability of batteries [11,12]. To overcome some of these limitations, neutral and near-neutral electrolytes have been proposed to improve cycling life and reversibility, with early studies focusing on NH_4Cl-based electrolytes originally used in primary ZABs [4].

Goh et al. [13] introduced a neutral NH_4Cl-based electrolyte with polyethylene glycol, demonstrating significant improvements in battery performance by enhancing Zn plating behavior and suppressing side

* Corresponding author.
E-mail address: y.durmus@fz-juelich.de (Y.E. Durmus).

https://doi.org/10.1016/j.ensm.2025.104862
Received 17 November 2025; Received in revised form 21 December 2025; Accepted 31 December 2025
Available online 1 January 2026

reactions compared to electrolytes without additives. In other work, Sumboja et al. [14] further reported the role of additives, by incorporating thiourea to improve the uniformity of Zn plating and extend cycle life to 540 cycles. Further insights, Clark et al. [15] demonstrated pH-dependent Zn ion coordination by conducting thermodynamic studies on NH_4Cl-$ZnCl_2$ electrolytes, revealing how pH affects Zn plating behavior.

Based on these findings, recent studies have shifted toward NaCl-based neutral electrolytes, which offer advantages such as lower volatility and reduced ammonia-related side reactions [16–19]. Although these showed improvements, a significant drawback of Cl^--containing electrolytes is the formation of Simonkolleite ($Zn_5(OH)_8Cl_2{\cdot}2H_2O$), which passivates the Zn anode and increases polarization during cycling and compromise electrochemical stability [4,15,17,20].

Electrolyte additives have been explored to stabilize Zn anode and regulate Zn plating by modulating the solvation shell of Zn ions [21–27]. Recent advances in electrolyte engineering have shown that amino-acid–based complexing agents offer a distinct and promising alternative to conventional organic or inorganic additives in zinc-based batteries [28,29]. Unlike the conventional additives, amino acids simultaneously provide metal-ion coordination, pH buffering, and interfacial regulation through their amphoteric properties, enabling more controlled Zn^{2+} solvation and suppressing parasitic reactions such as hydrogen evolution and surface passivation [30,31]. For example, Wang et al. [6] demonstrated that adding amphoteric amino acids to the alkaline electrolyte effectively regulates the zinc-ion solvation shell and stabilizes the Zn/electrolyte interface, thereby suppressing dendrite growth, hydrogen evolution, and by-product formation. As a result of this solvation and interfacial engineering, the modified electrolyte enables long-cycle, highly reversible Zn metal anodes which result in significantly improved cycling stabilities. In another study, Guerrero et al. [17] demonstrated that incorporating EDTA into a near-neutral NaCl electrolyte significantly alters Zn^{2+} solvation behavior, by chelating Zn^{2+} ions, EDTA suppressed the formation of Simonkolleite. Overall, electrolyte engineering through the use of suitable additives generally reduces zinc plating and stripping overpotentials, thereby leading to enhanced long-term electrochemical stability [8,20–22].

These studies emphasize the crucial impact of modified solvation shell between Zn^{2+}-complexing agents on electrochemical performance. In aqueous electrolytes, Zn^{2+} primarily exists as $[Zn(H_2O)_6]^{2+}$, forming a strongly bound solvation shell due to hydration interactions [20,32–34]. While this solvation behavior is important, it poses several challenges that negatively impact battery performance. First, the tightly bound solvation shell around Zn^{2+} limits ion mobility, leading to non-uniform Zn plating and uncontrolled dendrite growth. Uneven Zn plating can cause short circuits and battery failure. Second, this strongly coordinated hydration shell also introduces an energy barrier to desolvation, which may hinder plating kinetics and reduce electrochemical reversibility. Finally, the hydrated Zn^{2+} species interact with chloride and hydroxide ions in the electrolyte, facilitating the formation of Simonkolleite as a side reaction. While previous studies have demonstrated that electrolyte additives can influence Zn^{2+} solvation behavior, a comprehensive understanding of how these modifications affect Zn plating behavior, suppress side reactions, and enhance long-term cycling stability remains lacking.

Herein, we investigate a near-neutral electrolyte composed of 2 M NaCl solution (pH=10) with complexing agents such as glycine (Gly) and iminodiacetic acid (IDA), which are designed to regulate Zn^{2+} complexation behavior. The introduction of Gly or IDA not only stabilizes the electrolyte pH but also suppresses side product formation and improves cycling stability. To elucidate the underlying mechanisms, we employ electrochemical analysis, spectroscopic characterization, in-operando X-ray computed tomography (XCT), and density functional theory (DFT) calculations. These investigations reveal the critical role of complexing agents in modulating Zn^{2+}-complexes and enhancing the performance of Zn-air batteries. Ultimately, this work provides valuable insights into electrolyte additives for advancing next-generation aqueous ZAB system.

2. Results and discussion

2.1. Influence of complexing agents on the open circuit potentials

We employed 2 M NaCl aqueous electrolyte (pH=10) with 0.5 M glycine (Gly) or iminodiacetic acid (IDA) as complexing agents. These complexing agents contain both carboxylate and amino functional groups, enabling the coordination Zn^{2+} ions, modifying the solvation shell of Zn^{2+}-H_2O complexes [6,22,23,35]. The protonation state of the complexing agent, which is pH-dependent, plays a crucial role in determining its complexation behavior, i.e., Gly has two relevant pKa values: 2.35 (carboxylic acid group, –COOH) and 9.75 (protonated amino group, $–NH_3^+$) [36]. At pH 10, Gly predominantly exists in its zwitterionic form, with a deprotonated carboxylate group ($–COO^-$) and a neutral amino group ($–NH_2$), allowing it to act as a bidentate ligand site. On the other hand, IDA has two carboxylic acid groups with pKa values of 2.98 and 9.89 [37]. At pH 10, both groups are deprotonated to form carboxylate anions ($–COO^-$), while the amino group remains neutral ($–NH_2$), resulting in a tridentate coordination site (Fig. 1(a)).

The effect of complexing agents on the electrochemical behavior of Zn^{2+} was first evaluated through open-circuit potential (OCP) measurements over 24 hours (Fig. 1(b)). The cell with 2 M NaCl aqueous electrolyte (neat) exhibited an initial OCP of approximately -1.05 $V_{Ag/AgCl}$, which gradually decreased over time. In contrast, 2 M NaCl with 0.5 M Gly or 0.5 M IDA electrolytes initially showed more negative OCP values ($\sim$ -1.38 $V_{Ag/AgCl}$), stabilizing at -1.33 $V_{Ag/AgCl}$ after 24 hours without significant pH drop (2 M NaCl+ 0.5 M pH_{Gly}: 9.83, and 2 M NaCl+ 0.5 M pH_{IDA}: 9.77). The enhancement in potential can be attributed to Zn^{2+} complexation with the complexing agents, which stabilize Zn^{2+} through chelation and reduce its free ionic activity [17].

To investigate the interaction between Zn^{2+} ions and the complexing agents, UV–Visible spectroscopy was performed using 0.5 M Gly or IDA-containing electrolytes with $ZnCl_2$ as the Zn^{2+} source. Although a concentration of 0.1 M $ZnCl_2$ was used in other electrochemical measurements, the corresponding UV–Vis spectra exhibited absorbance values exceeding the linear detection range of the instrument (Figure S1). Therefore, a reduced concentration of 0.01 M $ZnCl_2$ was used in Fig. 1(c) to ensure accurate absorbance measurements within the instrument's valid range. For the 2 M NaCl with 0.5 M Gly electrolyte, a strong absorption band centered at 225 nm was observed, corresponding to the $n\rightarrow\pi^*$ electronic transition associated with the lone pair electrons on the carboxyl group [23,38,39]. After adding of 0.01 M $ZnCl_2$, the absorbance intensity significantly decreased, indicating coordination-induced suppression of this transition. This phenomenon suggests the complexation of Zn^{2+} with either the carboxylate or the amine functionalities of Gly, reducing the availability of non-bonding electrons involved in the transition.

A similar trend was observed in 0.5 M IDA-containing electrolyte (Fig. 1(c)). This electrolyte exhibited a distinct UV absorption peak at 235 nm. A slight bathochromic shift to Gly-containing electrolyte was observed, indicating coordination of the chelating agent to Zn^{2+} ions. This shift likely results from the stabilization of $n\rightarrow\pi^*$ transitions, facilitated by electron-donating atoms at the bidentate binding sites, such as carboxylate and secondary amine group [38,39]. Upon Zn^{2+} addition, the absorbance intensity was notably quenched, due to the formation of a Zn^{2+}–IDA complex.

Further investigations of the complexation was examined through Raman spectroscopy, as shown in Fig. 1(d–e). Characteristic vibrational shifts observed in the 760–850 cm^{-1} and 1200–1400 cm^{-1} regions provide clear evidence of Zn^{2+} coordination with the complexing agents. In the 760-850 cm^{-1} region (Fig. 1(d)), a single vibrational peak appears at 805 cm^{-1} (2 M NaCl + 0.5 M Gly) and 800 cm^{-1} (2 M NaCl + 0.5 M IDA), corresponding to C-N stretching and CO_2 rocking modes, which

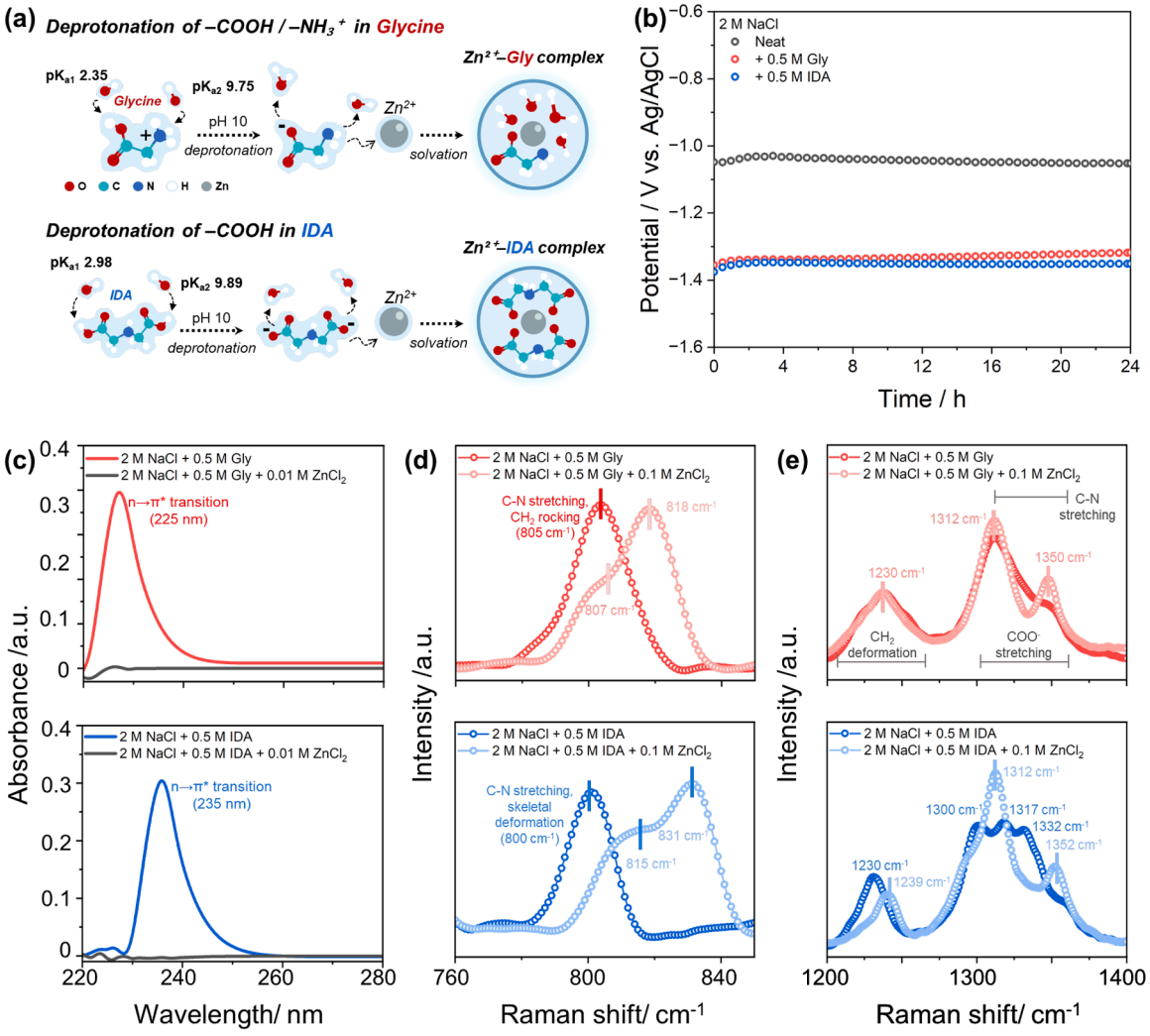

Fig. 1. **(a)** Schematic illustration of Zn^{2+} complexation with Gly and IDA in 2 M NaCl electrolyte (pH 10). (b) Open circuit potential (OCP) profile in three different electrolytes (black: 2 M NaCl (neat), red: + 0.5 M Gly, and blue: + 0.5 M IDA). (c) UV–Vis spectra of 2 M NaCl + 0.5 M Gly (red) and + 0.5 M IDA (blue) without/with 0.01 M $ZnCl_2$ (gray). Raman spectra of (d) in range of 760-850 cm^{-1}, and (e) 1200-1400 cm^{-1} of 2 M NaCl with 0.5 M Gly (red) and IDA (blue) with 0.1 M $ZnCl_2$.

arise from localized vibrational motions within the simple amino acid [40,41]. In IDA-containing electrolyte, the peak is associated with C-N stretching coupled with skeletal deformation, reflecting the more extended and delocalized nature of the IDA, where the nitrogen is symmetrically flanked by two carboxylate groups.

After introducing of 0.1 M $ZnCl_2$, the original 805 cm^{-1} peak shifted to ~807 cm^{-1}, accompanied by a shoulder at 818 cm^{-1} in Gly-containing electrolyte. This result suggests the formation of Zn^{2+}-Gly complexes involving different coordination modes through the carboxylate or amine groups. In contrast, the IDA-containing electrolyte shows a more pronounced transformation. The initial peak (800 cm^{-1}) shifted and split into two peaks at 815 and 831 cm^{-1}, indicating a vibrational mode splitting. This shows the stronger binding strength and chelation ability of IDA to Zn^{2+}. In the 1200-1400 cm^{-1} region (Fig. 1(e)), distinct changes are observed after the addition of $ZnCl_2$. In the Gly-containing electrolyte, the pre-existing peaks at 1312 and 1350 cm^{-1} exhibit clear splitting, reflecting vibrational mode separation caused by formation of Zn^{2+}-Gly complexes. In contrast, IDA-containing electrolyte initially shows three distinct peaks (1300, 1317, 1332 cm^{-1}), which are attributed to the asymmetric environments of the two carboxylate groups and amine functionality. After Zn^{2+} addition, these three peaks converge into a single peak at 1312 cm^{-1}, accompanied by a general shift in the surrounding spectral region. This transformation suggests that Zn^{2+} binding induces a more symmetric and stabilized coordination environment, consistent with the formation of bidentate or tridentate Zn^{2+}-IDA complexes.

2.2. Corrosion behavior of Zn with complexing agents

To evaluate the effect of complexing agents (Gly or IDA) on the corrosion behavior of Zn, potentiodynamic polarization measurements were conducted in neat, with 0.5 M Gly and 0.5 M IDA-containing electrolytes (Fig. 2(a)). The polarization curves obtained from -1.6 to -0.6 $V_{Ag/AgCl}$ at a scan rate of 5 mV s^{-1} reveal distinct electrochemical behaviors. Tafel analysis showed that the corrosion potential (E_{corr}) of Zn in neat electrolyte was -1.25 $V_{Ag/AgCl}$, while it shifted negatively to -1.39 $V_{Ag/AgCl}$ in both Gly and IDA-containing electrolytes. This negative shift indicates that Zn dissolution is more favorable in the presence of complexing agents due to the modified Zn-complex formation and the metallic surface being available for further oxidation.

This trend is further supported by the enhanced corrosion current densities (j_{corr}) that are increased to 29.8 μA cm^{-2} (Gly-containing electrolyte) and 20.4 μA cm^{-2} (IDA-containing electrolyte), compared to 9.8 μA cm^{-2} (neat electrolyte). These higher j_{corr} values indicate enhanced Zn dissolution, suggesting that the complexing agents influence Zn surface reactions and may reduce the extent of passivation layer formation. All electrolytes possess first a peak, and then a shoulder, followed by an abrupt increase in current density at more anodic

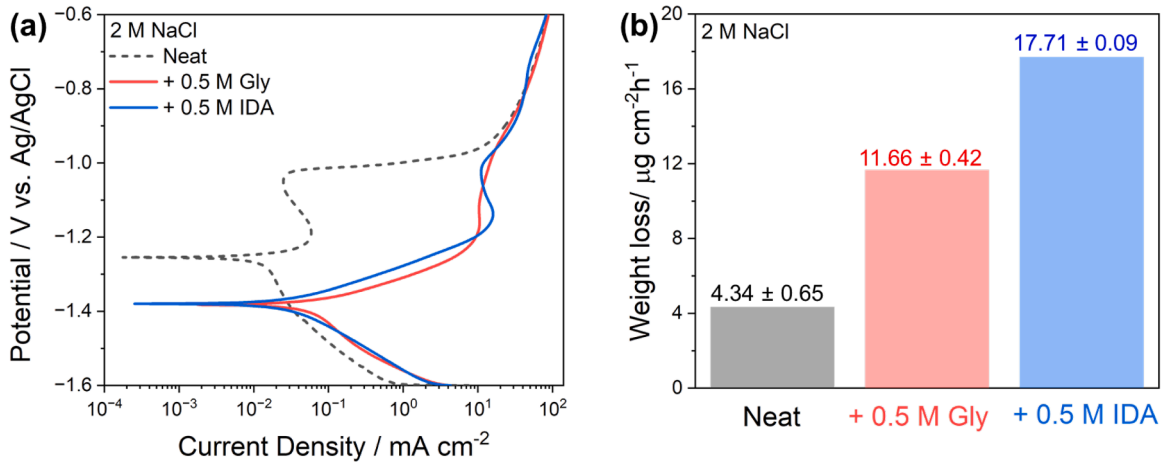

Fig. 2. **(a)** Potentiodynamic polarization of Zn in various electrolytes (dashed line: 2 M NaCl (neat), red: 2 M NaCl + 0.5 M Gly, and blue: 2 M NaCl + 0.5 M IDA). (b) Gravimetric weight loss after 7 days (gray: 2 M NaCl (neat), red: 2 M NaCl + 0.5 M Gly, and blue: 2 M NaCl + 0.5 M IDA).

potentials. In the neat electrolyte, this peak is observed at -1.2 $V_{Ag/AgCl}$, while it shifted to -1.1 $V_{Ag/AgCl}$ in Gly and IDA-containing electrolytes. This peak is associated with the layer formation on Zn surface [17]. At more anodic potentials, a sharp increase in current density indicates the pitting behavior initiated by chloride ions, beginning at around -1.0 $V_{Ag/AgCl}$ ($E_{pitting}$) [17,42].

The decrease on the current densities between E_{corr} (-1.25 $V_{Ag/AgCl}$) and $E_{pitting}$ (-1.0 $V_{Ag/AgCl}$) indicates the presence of a passive film in neat

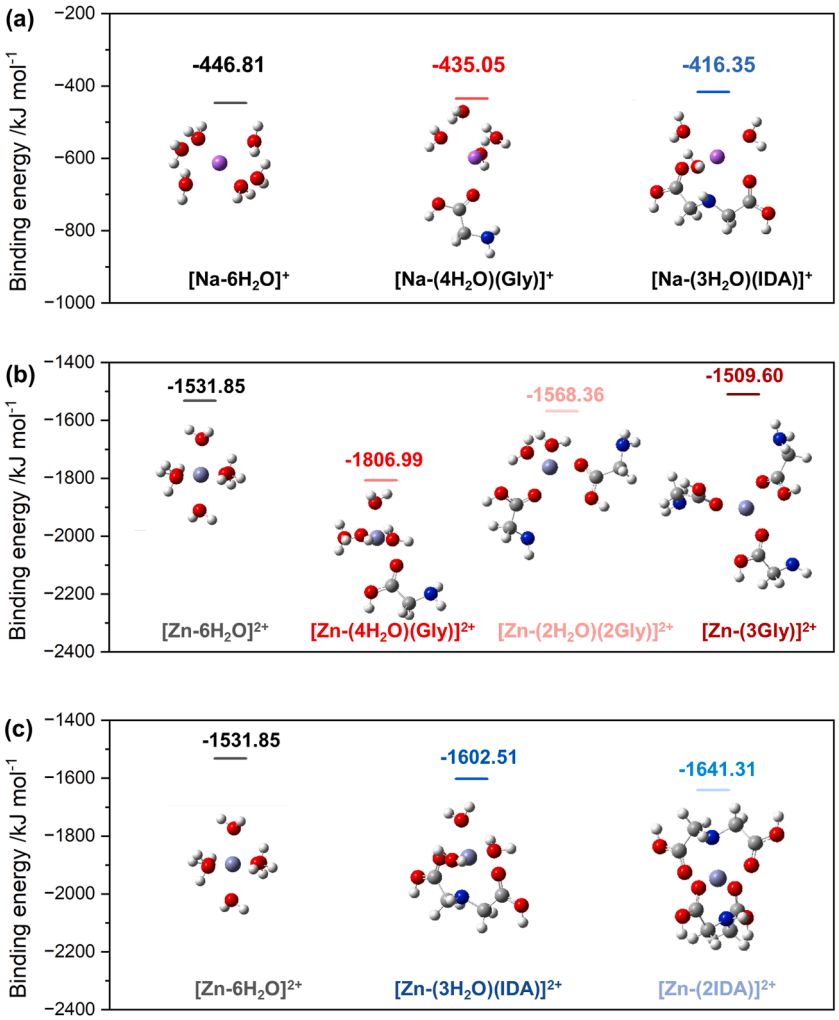

Fig. 3. DFT-calculated binding energies of Na^+ and Zn^{2+} with water, Gly, and IDA . (a) Binding energies of Na^+ in $[Na(H_2O)_6]^+$, $[Na(H_2O)_4(Gly)]^+$, and $[Na(H_2O)_3(IDA)]^+$. (b) Binding energies of Zn^{2+} with Gly in $[Zn(H_2O)_6]^{2+}$, $[Zn(H_2O)_4(Gly)]^{2+}$, $[Zn(H_2O)_2(Gly)_2]^{2+}$, and $[Zn(Gly)_3]^{2+}$. (c) Binding energies of Zn^{2+} with IDA in $[Zn(H_2O)_6]^{2+}$, $[Zn(H_2O)_3(IDA)]^{2+}$, and $[Zn(IDA)_2]^{2+}$.

electrolyte. In contrast, the presence of Gly or IDA results in a less distinct passivation peak but more negative E_{corr} and larger current densities in the range between E_{corr} and $E_{pitting}$. At more cathodic potentials (< -1.37 $V_{Ag/AgCl}$), water reduction becomes dominant, generating OH^-, which leads to local alkalization and cathodic corrosion [17,43]. Despite the near-neutral pH, localized increases in pH can promote cathodic corrosion and influence Zn surface state. Prestat et al. [44] reported that under extended polarization, metallic Zn stabilized at potentials below -1.27 $V_{Ag/AgCl}$. In contrast, ZnO and Simonkolleite formed at -1.04 $V_{Ag/AgCl}$, -1.26 $V_{Ag/AgCl}$ and above -1.01 $V_{Ag/AgCl}$, respectively. These findings indicate that Zn electrochemical behavior strongly depends on the applied potential and polarization duration.

Gravimetric weight loss analysis provides further insights into corrosion behavior (Fig. 2(b)). Zn weight loss rate was lowest in the neat electrolyte (4.34 ± 0.65 μg cm^{-2} h^{-1}) and significantly higher in Gly (11.66 ± 0.42 μg cm^{-2} h^{-1}) and IDA (17.71 ± 0.09 μg cm^{-2} h^{-1})-containing electrolytes. These results align with the polarization data, confirming that Gly and IDA increase Zn dissolution. The increased corrosion rate is attributed to the chelating effect of Gly and IDA, which coordinate with Zn^{2+} ions and suppress the formation of stable passivation layers, maintaining a more active surface. Although passivation mitigates excessive corrosion, it also limits electrochemical activity. Thus, complexing agents help preserve an active Zn metallic surface during battery operation by suppressing passivation.

2.3. Computational investigation of solvation energy between Zn^{2+}-complexing agents

Density functional theory (DFT) calculations were performed to investigate the complexation behavior of Na^+, H_2O, and Zn^{2+} with Gly or IDA to study their metal-complex structures in the electrolytes. As shown in Fig. 3(a), Na^+ preferentially coordinates with six water molecules to form $[Na\text{-}6H_2O]^+$, exhibiting the most favorable binding energy of -446.81 kJ mol^{-1}. In comparison, the substitution of water molecules with Gly or IDA leads to less favorable solvation energies, suggesting that Na^+ strongly prefers to stay in the form $[Na\text{-}6H_2O]^+$ configuration. As a result, Gly and IDA are expected to remain uncoordinated in the electrolyte before Zn^{2+} introduction.

Upon the introduction of Zn^{2+} during the oxidation process, Zn^{2+} formed the $[Zn\text{-}6H_2O]^{2+}$ with -1531.85 kJ mol^{-1}. DFT calculations revealed that Zn^{2+} exhibits significantly higher binding energy than Na^+. This difference arises from the electrostatic shielding effect related to the differences in radii and charge density between Na^+ and Zn^{2+} [45,46]. Interestingly, in Gly-containing electrolyte, Gly coordinates with Zn^{2+} to form $[Zn\text{-}(4H_2O)(Gly)]^{2+}$ complex, which exhibits a lower solvation energy (-1806.99 kJ mol^{-1}) than the fully hydrated $[Zn\text{-}6H_2O]^{2+}$ complex, indicating that Zn^{2+}-Gly complex is thermodynamically more stable (Fig. 3(b)).

In the IDA-containing electrolyte (Fig. 3(c)), the most stable complex is $[Zn\text{-}(2IDA)]^{2+}$ (-1641.31 kJ mol^{-1}), where two IDA molecules entirely replace water molecules in the Zn^{2+} solvation shell. Each IDA coordinates via functional groups, forming multidentate chelates with Zn^{2+}. The Zn^{2+}-IDA complex exhibits greater thermodynamic stability than $[Zn(H_2O)_6]^{2+}$ and $[Zn(H_2O)_3(IDA)]^{2+}$ complexes, indicating that in the presence of IDA, Zn^{2+} species preferentially form $[Zn(IDA)_2]^{2+}$ species in solution.

These DFT calculations suggest a solvation shell behavior in the electrolyte with complexing agents. Gly and IDA remain largely free in the initial NaCl electrolyte but strongly coordinate with Zn^{2+} once introduced, stabilizing it in a ligand-bound form less likely to undergo hydrolysis and precipitation. The ability of these ligands to form inner-sphere coordination complexes not only modulates Zn^{2+} complexation behavior but also plays a crucial role in suppressing the formation of insoluble Simonkolleite during cycling.

2.4. Electrochemical performance and surface analysis of Zn anodes

The electrochemical performance of Zn anodes was evaluated through galvanostatic stripping in half-cell and discharge in full-cell configurations to assess the effects of Gly and IDA on Zn oxidation behavior. Half-cell stripping tests were performed under galvanostatic current densities of 0.1, 0.25, 0.5, and 1 mA cm^{-2} in 2 M NaCl (neat) with 0.5 M Gly or IDA electrolytes. The stripping potentials in the Gly or IDA-containing electrolytes were approximately 280 mV more negative than those in the neat electrolyte, stabilizing at -1.29 $V_{Ag/AgCl}$ (2 M NaCl + 0.5 M Gly) and -1.28 $V_{Ag/AgCl}$ (2 M NaCl + 0.5 M IDA) as shown in Fig. 4(a), (b), and Figure S2.

The more positive stripping potential observed in the neat electrolyte, consistent with previous studies, [39,47] is attributed to the passive state of the surface and poor pH stability, which negatively impacts Zn electrochemical kinetics and the type of the reaction products.

To explore the relationship between pH stability and Zn stripping performance, post-stripping pH values were recorded after 24 hours of stripping at 1 mA cm^{-2}. In the neat electrolyte, the pH decreased from 10 to 6.6, coinciding with the formation of white, flake-like precipitates (Figure S3), which were identified as insoluble Zn-based species. In contrast, the Gly and IDA-containing electrolytes maintained a stable pH (~10), with no visible precipitation observed. This suggests that Gly and IDA effectively coordinate Zn^{2+} ions, preventing their reaction with OH^- and Cl^- ions, which would otherwise contribute to the formation of Zn $(OH)_2$ and Simonkolleite.

To further evaluate the long-term pH stability of the electrolytes, ex-situ pH measurements were conducted after galvanostatic stripping at 1 mA cm^{-2} for extended durations of 24 h and 100 h (Figure S4). While the pH of the neat electrolyte decreased to 6.6 after 24 h of stripping, the electrolytes containing Gly or IDA maintained remarkably stable pH values even after 100 h. These results demonstrate that the complexing agents provide effective buffering of the electrolyte environment, thereby mitigating pH-driven side reactions during prolonged electrochemical operation.

To investigate long-term stripping behavior, galvanostatic tests were performed at 1 mA cm^{-2} with a cut-off potential of -0.5 $V_{Ag/AgCl}$ (Fig. 4(c)). Surprisingly, after approximately 200 h of stripping, Gly or IDA-containing electrolyte exhibit a potential shift comparable to the neat electrolyte, suggesting that all complexing agents have been consumed by complexation with Zn^{2+}-Gly or IDA.

To clarify the optimal complexing agent concentration, additional concentration-dependent electrochemical analyses were performed. At lower concentrations (0.1 M), the limited amount of complexing agent was rapidly depleted through Zn^{2+} coordination, resulting in a loss of interfacial stabilization and a rapid shift of the stripping potential towards the neat electrolyte (Figure S5). In contrast, increasing the concentration of 0.5 M provides a sufficient complexing capacity to regulate Zn^{2+} complexation and maintain a stable interfacial regulation. This behavior is reflected in concentration-dependent electrochemical impedance spectroscopy (EIS) measurements (Figure S6 and Table S1), which indicate that the interfacial impedance response is most stable at the concentration of 0.5 M. At 0.1 M, the limited complexing-agent availability hinders interfacial regulation, whereas further increasing the concentration to 1.0 M does not provide additional stabilization and instead results in less well-defined impedance responses most likely due to increased electrolyte viscosity and associated ion-transport limitations.

Table 1 summarizes the mass utilization efficiency, practical capacity, and specific energy calculated after the long-term stripping experiments. These calculations were based on the total mass loss of the zinc electrodes. Stripping the electrodes in the presence of complexing agents yielded very similar results: efficiencies around 93% and specific capacities of approximately 770 mAh g_{Zn}^{-1}. Although similar values were also calculated for the neat electrolyte, the presence of insoluble reaction products may have exaggerated these results. The main advantage

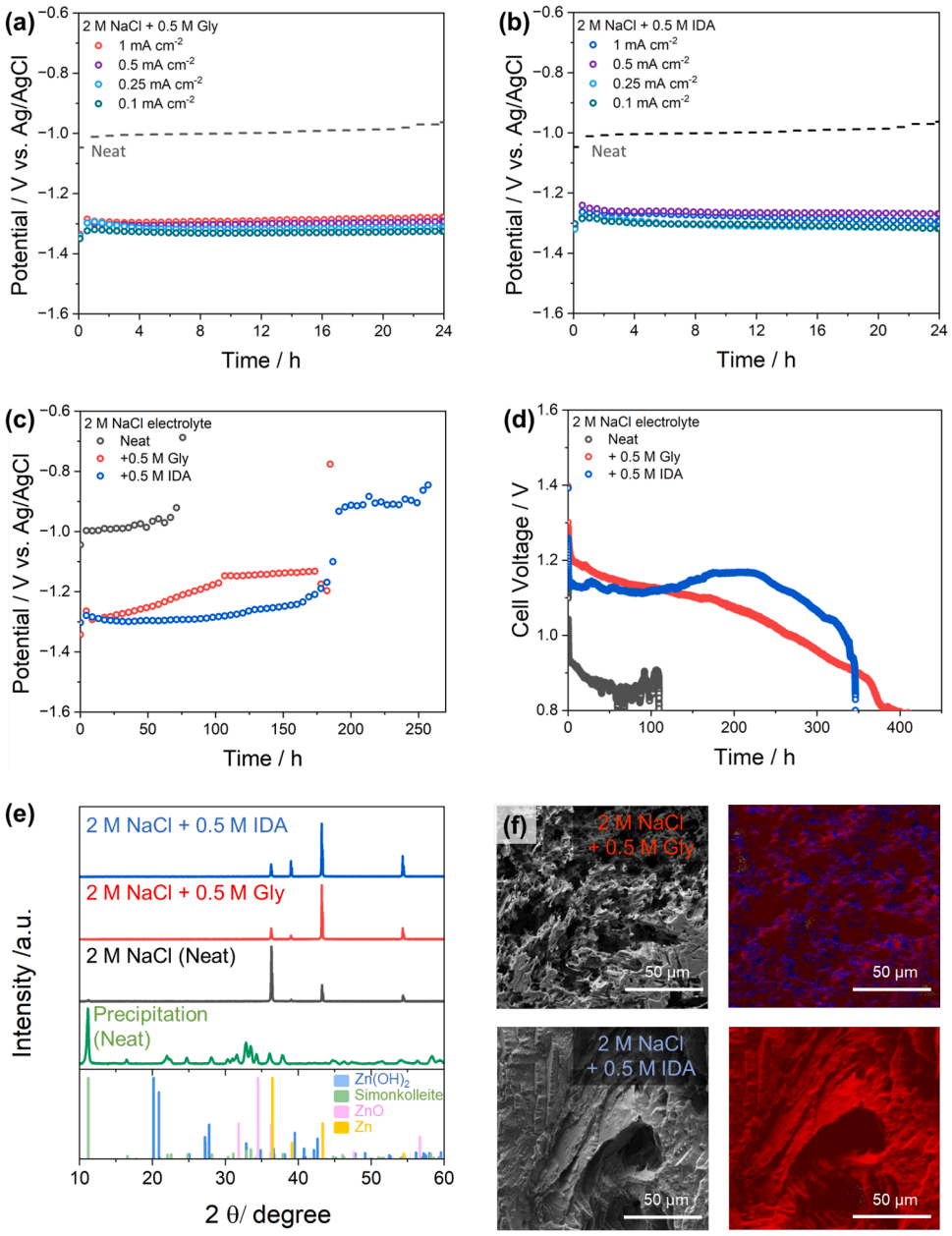

Fig. 4. Galvanostatic stripping profile in 2 M NaCl electrolyte with (a) 0.5 M Gly and (b) 0.5 M IDA complexing agents at various current densities. (c) Long term stripping profiles using 2 M NaCl (gray), + 0.5 M Gly (red), and + 0.5 M IDA (blue). (d) Galvanostatic full-cell discharge profiles of Zn-air full cells with 2 M NaCl (gray), + 0.5 M Gly (red), and + 0.5 M IDA (blue). (e) XRD patterns of Zn surface after 24 h stripping in half-cell configuration using neat (gray), + 0.5 M Gly (red), + 0.5 M IDA (blue), including the identified precipitation product in the neat electrolyte (green). (f) SEM images and corresponding EDX mapping results of the Zn anode surface in electrolyte with Gly-containing electrolyte (top) and IDA-containing electrolyte (bottom).

Table 1
Mass utilization efficiency, practical capacity, and practical specific energy values calculated after full-stripping process.

Electrolyte	Mass utilization efficiency (%)	Practical capacity (mAh g_{Zn}^{-1})	Practical specific energy (Wh kg_{Zn}^{-1})
2 M NaCl (neat)	91.3 ± 2.3	748.4 ± 18.7	611 ± 28.2
+ 0.5 M Gly	94.6 ± 0.4	775.2 ± 3.1	852.7 ± 3.4
+ 0.5 M IDA	92.8 ± 2.4	761.0 ± 26.7	852.3 ± 29.9

of using complexing agents is evident in the specific energies, which can reach up to 852 Wh kg_{Zn}^{-1}.

Furthermore, the amount of Zn^{2+} complexed by the complexing agents was estimated based on the stripping capacity of the cell (Table 1). The complexation number refers to the number of complexing agent molecules that bind to a single Zn^{2+} ion. The calculated complexation number for Zn^{2+} in Gly and IDA-containing electrolytes are 1.5 and 2, respectively (Supplementary Calculation 1), whereas DFT calculations predict a complexation number of 1:1 (Gly) and 1:2 (IDA). This difference likely arises from the simplified assumptions of DFT models compared to the dynamic nature of electrochemical environments. DFT calculations describe an isolated system where Zn^{2+} forms the most stable complex, whereas, in solution, Zn^{2+} interacts with multiple species, undergoes ligand exchange, and forms transient coordination states. Furthermore, the protonation state of the complexing agent at pH 10 plays a role in complexation behavior. Gly exists as a

mixture of zwitterionic and deprotonated forms, both capable of Zn^{2+} complexation [22,45]. IDA remains partially protonated, with its carboxyl groups exhibiting pH-dependent flexibility that allows for mixed complexation structures [48]. These factors contribute to the difference between experimentally determined and DFT-predicted complexation number.

Furthermore, full-cell configurations were tested to assess the practical applicability of ZABs (Fig. 4(d)). The neat electrolyte exhibited an initial open-circuit voltage (OCV) of ~1.1 V, gradually decreasing to the cut-off voltage of 0.5 V after 110 hours of discharge. In contrast, the Gly-containing electrolyte exhibited an initial OCV of 1.4 V, stabilizing at 1.2 V before gradually decreasing to 0.9 V after 360 hours and finally reaching the cut-off voltage at 530 hours of operation. The IDA exhibited similar behavior, with an initial OCV of 1.39 V, a stabilized discharge voltage of 1.17 V, and termination at 350 hours.

These results confirm that both Gly and IDA significantly improve the long-term electrochemical performance of ZABs. Despite the extended discharge durations in Gly and IDA-containing electrolytes, full-cell performance is also influenced by cathodic components, particularly air cathode stability and electrolyte-induced degradation. Figure S7(a), shows that prolonged discharge of the neat electrolyte leads to the formation of white precipitates, whereas electrolytes containing complexing agents remain clear and free of solids, consistent with the half-cell results. In the neat electrolyte, discharge termination arises from the formation of a surface-blocking white film on both electrodes. In contrast, for electrolytes with additives, the most likely cause of discharge termination is the depletion of the complexing agents, as evidenced by the corresponding voltage profiles.

XRD analysis was performed on Zn electrodes stripped for 24 hours at 1 mA cm^{-2} (Fig. 4(e)) to characterize the potential reaction products on the surfaces. Zn electrode stripped in the neat electrolyte exhibited additional peaks at ~10°, corresponding to the formation of Simonkolleite. In contrast, Zn electrodes stripped in Gly and IDA-containing electrolytes exhibited a more uniform metallic Zn surface, as confirmed by scanning electron microscopy (SEM) and energy-dispersive X-ray spectroscopy (EDX) analyses (Fig. 4(f) and Figure S8-10). EDX elemental mapping showed a significant reduction in oxygen and chlorine content, compared to that in the neat electrolyte (Figure S10), indicating that Gly and IDA-containing electrolytes suppress $Zn(OH)_2$ and Simonkolleite formation, thereby reducing the passivation of Zn surface.

To further investigate the effects of additive depletion, Zn electrodes were stripped under 0.1 M Gly and IDA-containing electrolytes and subsequently analyzed by post-mortem X-ray diffraction (XRD) (Figure S11). The XRD patterns reveal the formation of Simonkolleite due to the lack of complexing agents.

These results suggest that Gly and IDA alter Zn^{2+} interactions in solution by forming thermodynamically favorable coordination complexes, thereby reducing the availability of free Zn^{2+} from the hydration shell $[Zn(H_2O)_6]^{2+}$ and suppressing the formation of passivation layers and Simonkolleite during the stripping process.

2.5. Understanding of Zn plating behavior with complexing agents

In aqueous electrolytes, Zn plating often leads to dendritic growth, which can cause internal short circuits and significantly reduce the lifespan of Zn-based batteries. These issues can be mitigated by employing complexing agents that form stable and well-defined complexes with Zn^{2+} ions, thereby modulating ion availability and improving interfacial kinetics. To understand the role of pre-existing Zn^{2+} in the electrolyte, 0.1 M $ZnCl_2$ was added to simulate conditions where Zn^{2+} is already present. Nucleation overpotential is a key factor in controlling Zn plating uniformity, as a higher overpotential has been shown to reduce the critical nucleus size, leading to more uniform growth and effectively mitigating dendrite formation [49,50].

To investigate the influence of Gly and IDA on Zn nucleation and early-stage plating, nucleation overpotentials were first evaluated by applying a constant current density of 1 mA cm^{-2} (Fig. 5(a)). Gly-containing electrolyte exhibited a lower nucleation overpotential (22 mV) than IDA-containing electrolyte (93 mV). This suggests that Zn nucleation occurs more readily in the presence of Gly, likely due to its less sterically hindered structure and weaker interaction between Zn^{2+} and Gly, which reduces the energy barrier for initial ion reduction.

Additionally, EIS measurements were performed before plating, after 5 minutes, and after 60 minutes of plating (Fig. 5(b-c)). In both Gly and IDA-containing electrolytes, the charge-transfer resistance (R_{ct}) decreased over time (Table S2). Notably, the IDA-containing electrolyte consistently exhibited higher R_{ct} values than the Gly-containing electrolyte. This result aligns with the higher nucleation overpotential observed in the IDA-containing electrolyte, implying that Zn nucleation occurs under a larger energy barrier, which helps regulate the initial nucleation process [49,50].

To further quantify the influence of complexing agents on Zn^{2+} desolvation and interfacial charge-transfer kinetics, temperature-dependent EIS measurements were performed, and the activation energy (E_a) was extracted from the charge-transfer resistance using the Arrhenius relation (Figure S12), The Gly-containing electrolyte exhibited a lower E_a (7.99 kJ mol^{-1}), whereas the IDA-containing electrolyte showed a significantly higher E_a (10.96 kJ mol^{-1}). This result indicates that Zn^{2+} desolvation and interfacial charge transfer are energetically more demanding in the presence of IDA, consistent with its higher nucleation overpotential and large R_{ct} values.

Furthermore, morphological analysis using SEM (Fig. 5(d–e)) and laser scanning microscopy (LSM, Fig. 5 (f–g), Figure S13) further supported the electrochemical observations. In the Gly-containing electrolyte, the Zn plating layer consisted of relatively rough, aggregated grains with localized height variations and non-uniform surface features. Although no prominent dendritic structures were observed, the morphology suggests less controlled nucleation and growth behavior than IDA-containing electrolyte. In contrast, the Zn deposited from the IDA-containing electrolyte formed a compact, densely packed, and uniform layer, indicating more homogeneous plating.

DFT calculations further explain the difference in Zn plating behavior. As shown in Fig. 5(h) and Figure S14, the binding energies of Gly or IDA molecules on the Zn (001) surface were calculated to evaluate their affinity toward the metal interface. The calculated adsorption energy for Zn-IDA (-1.135 eV) was significantly lower than that of Zn-Gly (-0.926 eV) and hydrated Zn–H_2O (-0.289 eV), indicating a stronger interaction between IDA and the Zn surface.

This stronger binding of IDA may contribute to more stable and well-defined nucleation sites by modulating the local electrochemical environment. It likely promotes the formation of a more structured electrical double layer (EDL), which enhances charge transfer kinetics and suppresses local ion concentration fluctuations during plating [50]. In contrast, the weaker interaction of Gly with the Zn surface leads to less controlled nucleation, contributing to rougher, less compact Zn growth.

To directly examine changes in the interfacial electric double layer during Zn plating, the high-frequency region of the EIS spectra was analyzed using equivalent-circuit fitting, and the double-layer capacitance (C_{dl}) was extracted, with the results summarized in Table S2. In the Gly-containing electrolyte, C_{dl} increases markedly with plating time, indicating the development of a more diffusive and solvent-rich electric double layer [51]. This behavior is consistent with progressive interfacial roughening. In contrast, the IDA-containing electrolyte exhibits a continuous decrease in C_{dl} during Zn plating, reflecting the formation of a more compact and structured electric double layer. This trend is consistent with the larger high-frequency impedance contribution retained in the IDA electrolyte after prolonged plating. The reduced C_{dl} observed for the IDA-containing electrolyte therefore provides direct electrochemical evidence for the formation of a compact and ordered interfacial structure, supported by DFT calculations.

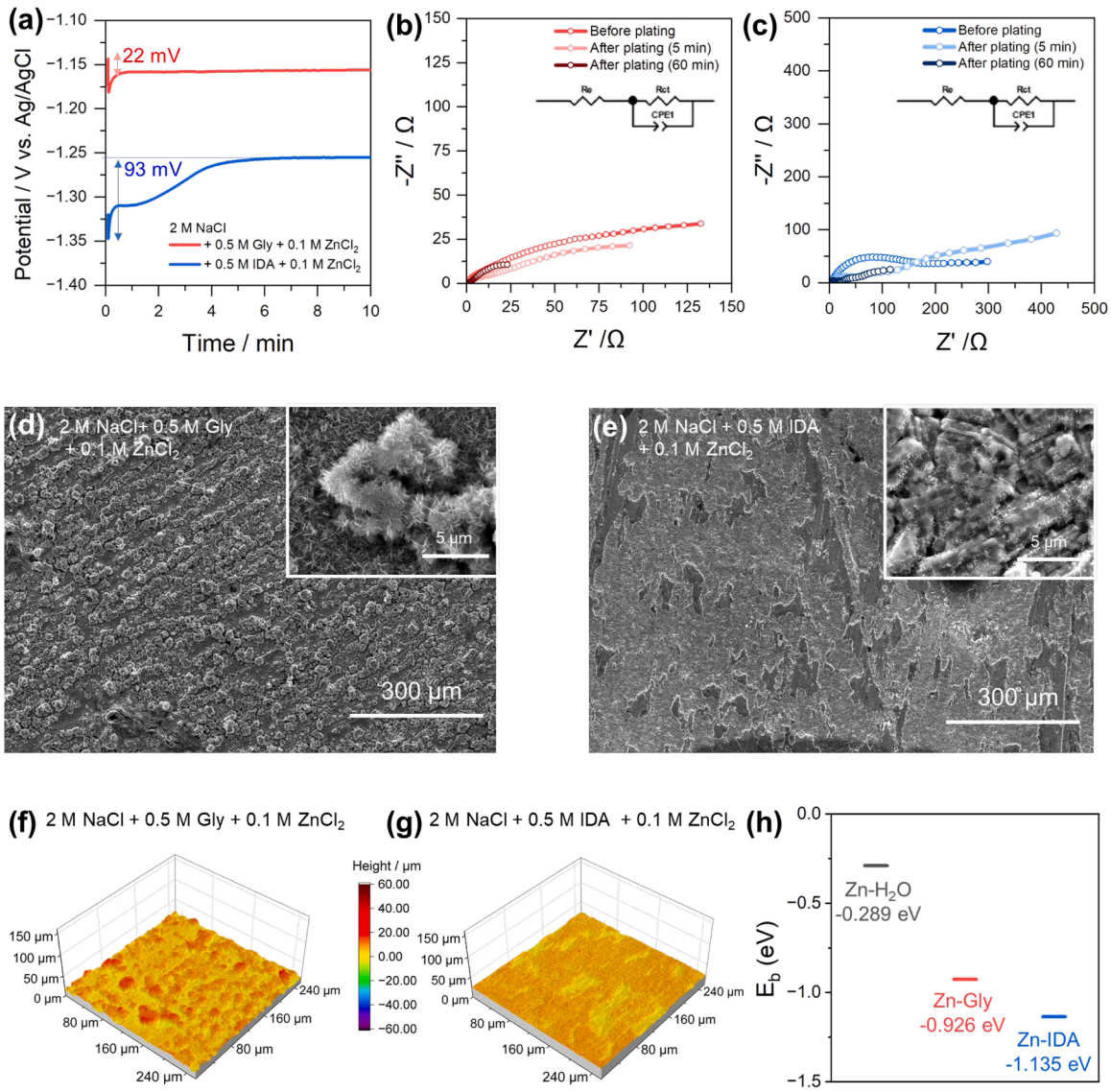

Fig. 5. (a) Nucleation overpotential profiles for 2 M NaCl with 0.5 M Gly (red) or 0.5 M IDA (blue) electrolytes containing 0.1 M $ZnCl_2$ under an applied current density of 1 mA cm^{-2}. (b,c) Nyquist plots of Zn electrodes recorded at open-circuit potential (before plating), after 5 minutes, and after 60 minutes of plating in (b) + 0.5 M Gly and (c) + 0.5 M IDA-containing electrolytes with 0.1 M $ZnCl_2$. (d,e) SEM images of Zn surface in 2 M NaCl + 0.5 M Gly (d) or + 0.5 M IDA (e) with 0.1 M $ZnCl_2$ after 2 mAh cm^{-2} plating process. (f,g) LSM images of Zn surface in 2 M NaCl + 0.5 M Gly (f) or + 0.5 M IDA (g) with 0.1 M $ZnCl_2$ after 2 mAh cm^{-2} plating process. (h) Binding energy between H_2O, Gly, and IDA molecule with Zn surface (001) obtained DFT simulation.

2.6. *In-operando XCT analysis of Zn plating-stripping behavior*

Zn plating-stripping behavior was investigated using in-operando X-ray computed tomography (XCT) in IDA or Gly containing electrolytes with 0.1 M $ZnCl_2$. XCT was employed to monitor Zn plating-stripping behavior in real-time, providing three-dimensional visualizations of morphology growth during the plating step, and reversibility during cycling. The measurements were performed on Zn||Zn symmetric cells using zinc wire (Ø = 0.5 mm) operated at a current density of 1 mA cm^{-2}. Detailed experimental conditions are described in the experimental method section and Table S3.

Fig. 6(a-b) shows the results of in-operando XCT analysis in the IDA-containing electrolyte. Zn growth rate was calculated from the evolution of the 3D structure obtained via XCT, as shown in Fig. 6(a). The cell was subjected to a total of seven plating cycles, with the first three performed at 1 mA cm^{-2}, and the subsequent four at 2 mA cm^{-2}, each with a fixed specific capacity of 4 mAh cm^{-2}. Each plating step was followed by 4 hours rest under open-circuit conditions to enable high-resolution 3D scanning. Fig. 6(a) presents the time-dependent growth rate of Zn (see [53] for further details), along with the applied current and predicted deposition rates. During the first three plating steps (①–③, at 1 mA cm^{-2}), the growth rate remained consistent and closely aligned with the predicted values, which ranged from approximately 10 to 35 μg h^{-1}. In the subsequent steps (④–⑦, at 2 mA cm^{-2}), the growth rate increased proportionally while still following the predicted trend.

The inset radiogram images in Fig. 6(a) present the Zn plating behavior following each plating step. This observation is further supported by the 3D reconstructed XCT images shown in Fig. 6(b), which depict the morphology of the Zn electrode after each plating step. The "pristine" image illustrates the initial state of the Zn wire surface. Following the initial plating cycle, mostly layer-like and few island-like Zn deposits were formed on the electrode surface. As the plating cycles continued, this initial layer gradually developed into a more uniformly dense Zn layer. In the later stages (cycles ④–⑦ at 2 mA cm^{-2}), the Zn layer remained uniform and dense, consistently expanding across the electrode surface while maintaining its structural integrity over the

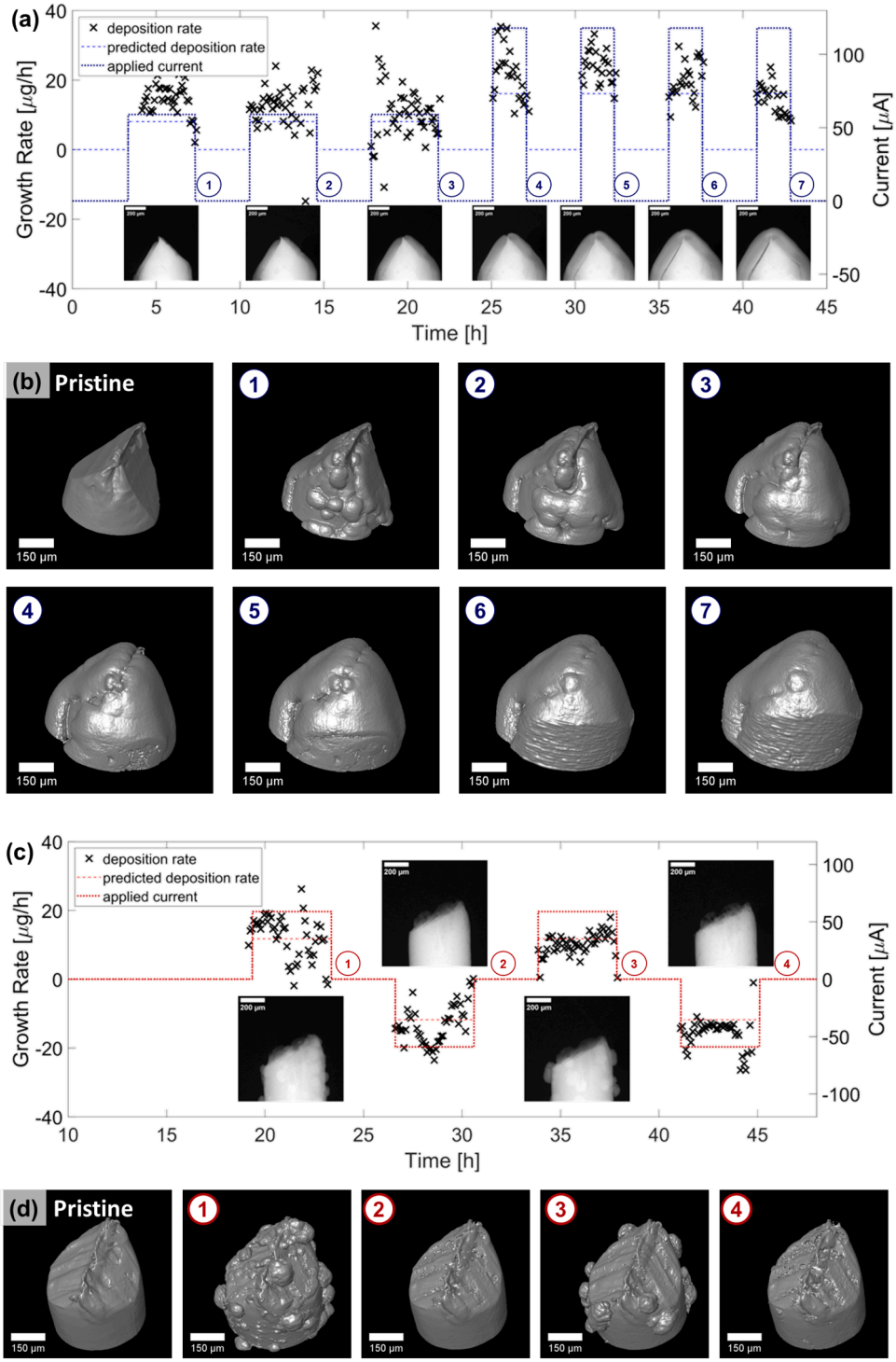

Fig. 6. In-operando XCT results (a) Zn growth rate and plating profiles of 2 M NaCl + 0.5 M IDA + 0.1 M $ZnCl_2$ with the overview radiogram images after each plating step, (b) corresponding 3D images after each plating step. (c) Cycling behavior with 2 M NaCl + 0.5 M Gly + 0.1 M $ZnCl_2$, and the overview radiogram images after each plating-stripping steps, (d) corresponding 3D images after each plating-stripping steps.

entire 21 mAh cm^{-2} plating process without showing any signs of dendritic growth. These results demonstrate that the IDA-containing electrolyte enables stable and uniform Zn layer formation during repeated plating steps, even under relatively higher current densities. The evolution of the surface during the plating experiments can also be seen in Video S1.

To further evaluate the behavior of Zn plating–stripping, a cycling test was conducted using the Gly-containing electrolyte, as shown in Fig. 6(c-d). Fig. 6(c) presents the Zn growth rate, which was calculated from XCT measurements during four plating–stripping cycles. Each cycle consists of a plating and stripping step, performed at a current density of 1 mA cm^{-2} with a fixed capacity of 4 mAh cm^{-2}. The growth rate profile in Fig. 6(c) reveals that Zn is deposited during the plating steps (① and ③), while the subsequent stripping steps (② and ④) exhibit effective stripping, as indicated by negative growth rates. This suggests that Zn is successfully removed during stripping, with minimal residual accumulation over the cycles. The inset radiogram images further illustrate this cycling behavior.

Fig. 6(d) displays the evolution of the Zn electrode morphology captured by 3D XCT after each plating–stripping step. After the first plating step (①), Zn deposition appears as many island-like structures of various sizes. The subsequent stripping step (②) effectively reverses the Zn plating, resulting in a surface morphology similar to the initial state. In the second plating step (③), Zn is redeposited in a similar manner although in fewer but more larger structures. The final stripping step (④) also achieves substantial Zn stripping from the previously plated Zn, indicating that the Gly-containing electrolyte supports relatively stable and reversible Zn plating–stripping behavior over multiple cycles. Under these conditions, stripping even at 1 mA cm^{-2} for 4 hours did not result in any visible pitting behavior that might potentially originate from the NaCl electrolyte. The changes in surface morphology during the cycling experiments can also be seen in Video S2.

While both Gly and IDA demonstrated effective Zn plating–stripping behavior, the low concentration of Zn^{2+} in the initial electrolyte formulations (2 M NaCl with 0.5 M IDA or Gly) made it challenging to clearly resolve early-stage deposition using XCT, as shown in Figures S15 and S16. Under these conditions, zinc plating was not distinctly visible, likely due to the limited spatial resolution of the measurement hindered the ability to clearly monitor the plating and stripping behavior during the early cycles. To address this limitation, 0.1 M $ZnCl_2$ was added to the electrolytes, allowing for more precise tracking of zinc plating.

Together with the findings in Fig. 5, these in-operando XCT results confirm the beneficial role of IDA and Gly in improving Zn plating-stripping behavior. IDA promotes highly uniform Zn nucleation and growth, while Gly, although yielding somewhat less homogeneous plating, still ensures structurally stable and reversible cycling.

2.7. Long-term cycling performance

The long-term cycling stability of Zn plating-stripping was evaluated using 2 M NaCl (neat), with 0.5 M Gly or 0.5 M IDA electrolytes under galvanostatic stripping-plating conditions (±1 mA cm^{-2}, 4 hours) over 65 cycles. All cycling experiments were performed in symmetrical-cell configurations, since the additives exhibited interactions with the commercial air electrode (see Figure S7(b)), and the development of a new air cathode lies beyond the scope of the present study.

As shown in Fig. 7(a), the neat electrolyte exhibited unstable potential fluctuations and a high overpotential, eventually leading to cell failure after 52 cycles. This instability is attributed to the formation of a passivation layer on the Zn electrode, as well as solid precipitates in the electrolyte, which reduce reversibility and cause pH instabilities. In contrast, electrolytes containing 0.5 M Gly or IDA displayed remarkably more stable electrochemical behavior. Both plating and stripping overpotentials remained relatively steady up to 65 cycles, with only minimal fluctuations.

During the initial 5 cycles, higher overpotentials were observed, ranging from 0.4 ~ 0.1 $V_{Ag/AgCl}$. This is possibly due to the very low concentrations of Zn-complexes, which make efficient plating challenging. However, these overpotentials gradually decreased and stabilized over continued cycling.

For the Gly-containing electrolyte, the average stripping potential remained relatively stable at approximately –1.24 $V_{Ag/AgCl}$, while the plating potential was initially stable but gradually shifted toward more positive values over extended cycling (–1.30 to -1.24 $V_{Ag/AgCl}$). In contrast, the IDA-containing electrolyte demonstrated even better stability in stripping-plating potentials. The stripping potential consistently remained near –1.30 $V_{Ag/AgCl}$, while the plating potential stabilized around –1.40 $V_{Ag/AgCl}$. Although the plating potential is less negative than that of the Gly containing electrolyte, it remained remarkably

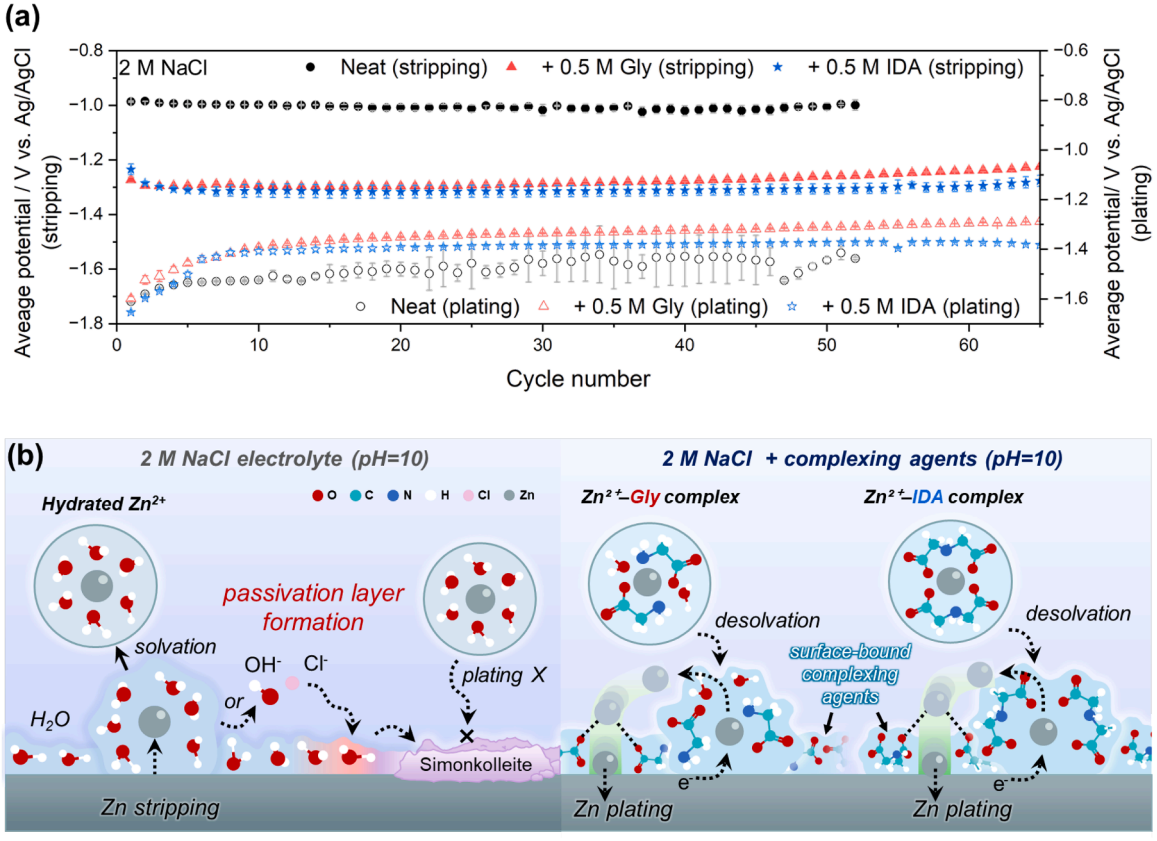

Fig. 7. (a) Long-term stripping-plating profile of Zn||Zn symmetric cell with neat, + 0.5 M Gly, or + 0.5 M IDA electrolyte at 4 mAh cm^{-2}. (b) Schematic of Zn^{2+} stripping-plating pathways and Zn^{2+} complex formation in 2 M NaCl (neat), + 0.5 M Gly, or +0.5 M IDA electrolytes.

stable until 65 cycles.

This stable plating behavior is attributed to the stronger interaction between IDA and the Zn surface, as demonstrated by DFT calculations and nucleation overpotential analysis presented in Fig. 5. The strong binding energy between IDA and Zn surface promotes the formation of a more structured EDL, facilitating improved charge transfer kinetics [51]. Additionally, the high binding affinity of IDA may contribute to a higher nucleation overpotential, thereby supporting uniform and controlled Zn deposition [6,26,49].

To further understand the high overpotential observed during the initial cycles, electrolyte samples were periodically collected throughout the cycling, and Zn^{2+} concentrations were quantified using ICP-OES analysis (Figure S17). The theoretical Zn^{2+} concentration was calculated based on the amount of Zn dissolved during the stripping process, without considering the plating step. In the neat electrolyte, the measured Zn^{2+} concentration was significantly lower than the calculated value, likely due to the formation of insoluble byproducts such as Simonkolleite, which traps Zn^{2+} and reduces its availability.

In both 0.5 M Gly or 0.5 M IDA-containing electrolytes, the measured Zn^{2+} concentration remained close to the theoretically calculated value during the stripping step over the first 100 hours (approximately 12 stripping–plating cycles). This indicates that Zn^{2+} was not effectively utilized during the plating process in this period, which may explain the relatively high overpotential observed in the early stages of cycling. After 100 hours, a noticeable decrease in Zn^{2+} concentration was observed, suggesting that more effective Zn plating and improved plating–stripping reversibility had begun. To confirm this behavior, the electrolytes collected after 100 hours of stripping were reused in a separate cycling test. The resulting overpotential profile closely matched with that observed after 100 hours of standard cycling (Figure S18–S19).

Post-mortem structural and morphological analyses of the cycled Zn electrodes were conducted by XRD and SEM/EDX after long-term Zn cycling to identify irreversible side products and interfacial changes associated with cell failure (Figure S20, and Figure S21). XRD patterns are dominated by metallic Zn for both Gly- and IDA-containing electrolytes, accompanied by only weak signals attributable to ZnO and Simonkolleite, suggesting that extensive irreversible passivation is largely suppressed within the reported cycling duration. SEM images and EDX mapping reveal that the Gly-containing electrolyte produces a rough and porous surface morphology, whereas IDA-containing electrolyte yields a more compact and uniform surface. Elemental mapping shows broadly distributed oxygen and localized chloride-containing regions, consistent with the minor secondary phases detected by XRD.

Based on these findings, a stripping-plating mechanism in electrolytes containing complexing agents is proposed, as illustrated in Fig. 7 (b). During the stripping process in the 2 M NaCl electrolyte, Zn is oxidized to Zn^{2+}, which then forms a hydrated solvation shell, typically represented as $[Zn(H_2O)_6]^{2+}$. These hydrated Zn^{2+} ions undergo hydrolysis, leading to the formation of insoluble byproducts such as Simonkolleite. The accumulation of these byproducts on the Zn surface results in passivation and pH instabilities, contributing to poor Zn reversibility and accelerated cell failure.

In contrast, the presence of complexing agents (Gly or IDA) facilitates the complexation with Zn^{2+}, wherein H_2O molecules in the solvation shell are partially or fully replaced. This modulation of complex formation reduces water-induced side reactions and enhances Zn^{2+} utilization during cycling. Initially, free complexing agents preferentially adsorb onto the Zn surface due to their strong binding energies, as confirmed by DFT calculations (Fig. 5(h)). Both IDA and Gly exhibit higher adsorption energies on the Zn surface compared to H_2O, allowing them to displace interfacial H_2O molecules and create a H_2O-deficient EDL. This modified EDL suppresses parasitic reactions and stabilizes the electrode-electrolyte interface [26].

During the plating process, the Zn-complexes are transported toward the Zn surface, where they undergo partial desolvation near the interface. The pre-adsorbed complexing agents (IDA or Gly) further interact with the incoming Zn^{2+} ions, stabilizing them at the surface and facilitating their reduction. This interaction increases the desolvation energy barrier, leading to a higher nucleation overpotential. However, it also promotes more defined and energetically stable nucleation behavior, enabling uniform and controlled Zn growth. This observation aligns with the stable plating potential and dense layered Zn morphology seen in the IDA-containing electrolyte.

A similar mechanism is proposed for Gly, which also binds more strongly to Zn than H_2O and contributes to improved interfacial stability. However, due to its comparatively lower binding strength and coordination tendency than IDA, Zn plating in the Gly-containing electrolyte exhibits slightly less uniformity and more variation in overpotential over long-term cycling.

To further understand the long-term cycling performance, the cyclability is compared with representative Zn-air batteries operating in near-neutral electrolytes reported in the literature. As shown in Table S4, the reported cycling stability spans a wide range of operating conditions, including electrolyte composition, areal capacity, and current density. The present system achieves stable cycling at a relatively high areal capacity of 4 mAh cm^{-2} using a simple NaCl-based electrolyte under demanding near-neutral conditions.

All in all, the long-term cycling results confirm the effectiveness of Gly and IDA as complexing agents to modulate the solvation environment in 2 M NaCl electrolyte. The addition of Gly and IDA suppresses passivation, enhances interfacial stability, and promotes high Zn reversibility. Notably, IDA facilitates the formation of uniform Zn layer during plating, contributing to stable voltage profiles. While Gly-containing electrolyte gradually increases plating potential over cycling, it still supports stable Zn stripping-plating behavior up to 65 cycles, demonstrating its promise as an effective complexing agent for improving Zn anode performance. Future work may focus on extending the complexing agent strategy to full-cell systems, particularly to mitigating cathodic side reactions with electrolyte and ensuring long-term electrochemical stability between complexing agents and the air cathode. These efforts could further improve cycling durability and discharge efficiency in Zn-air batteries.

3. Conclusion

In this study, we investigated the role of amino acid-based complexing agents, glycine (Gly) and iminodiacetic acid (IDA), in regulating the zinc complexes and improving the electrochemical performance of near-neutral NaCl-based electrolytes for aqueous Zn-air batteries. Through a combination of electrochemical characterization, spectroscopic analysis, density functional theory (DFT) calculations, and in-operando X-ray computed tomography (XCT), we demonstrate that both Gly and IDA effectively modulate the Zn^{2+} solvation environment via inner-sphere coordination, thereby mitigating Zn hydrolysis and suppressing the formation of insoluble byproducts such as Simonkolleite.

DFT calculations reveal enhanced thermodynamic stability of Zn^{2+}-amino acid complexes compared to hydrated Zn^{2+}, while in-operando XCT directly confirms that such solvation regulation leads to more uniform and reversible Zn plating and stripping behavior. Long-term cycling tests demonstrate that Gly and IDA-containing electrolytes significantly extended the operational life of Zn anodes compared to 2 M NaCl electrolyte.

Overall, this work demonstrates the role of amino acid-based complexing agents in modulating the Zn^{2+} solvation environment in near-neutral electrolytes. By stabilizing Zn^{2+} through coordination, Gly and IDA suppress passivation and improve the reversibility of Zn plating and stripping. Moreover, their interfacial interactions lead to more uniform Zn deposition, particularly in the IDA-containing electrolyte. This work indicates that solvation shell regulation provides a practical strategy for developing more stable aqueous Zn-based battery systems.

4. Experimental section

4.1. Materials

Zinc rod (4 N), and Iminodiacetic acid (> 98%) were purchased from Alfa Aesar. NaCl (>99.5%), Glycine (> 99%), and NaOH (> 97%) were obtained from Sigma-Aldrich. Deionized water was purified from a PURELAB Elga system (conductivity < 0.1 μS cm^{-1}), the air cathode (porous carbon on nickel mesh (E4 type)) was purchased from ElectricFuel Ltd.

4.2. The preparation of zinc electrode

Zinc rod was cut into discs with a thickness of 1.25 mm for electrode preparation. The zinc discs were then embedded in cold-mount epoxy (EpoFix, Struers), and the surface of zinc discs was ground using 800-grit SiC sandpaper before the electrochemical tests. The exposed electrode area was 1.327 cm^2.

4.3. The preparation of electrolyte

The electrolyte solutions were prepared by dissolving NaCl and additives (Gly or IDA) in deionized water, followed by purging with Ar gas for 10 minutes to remove dissolved oxygen. 2 M NaCl solution was prepared and adjusted to pH 10 using 1 M NaOH. Moreover, 0.5 M of each additive was added into the 2 M NaCl solution, and the pH was adjusted to 10 with the 1 M NaOH solution with the help of a dual pH/conductivity meter (Duo S213, Mettler Toledo). The same instrument was employed to monitor bulk pH variations by comparing the pH values of the solutions before and after the experiments.

4.4. Electrochemical characterization

For electrochemical characterization, a three-electrode half-cell system was used, consisting of a Zn working electrode, a Pt mesh counter electrode, and an Ag/AgCl reference electrode **(**Figure S22**)**. All electrochemical measurements were performed using a Biologic VMP 3 potentiostat (Biologic, France) at room temperature and 50% relative humidity.

The open-circuit potential (OCP) of each electrolyte was recorded over 24 hours. Potentiodynamic polarization measurements were conducted with a scan rate of 5 mV s^{-1} from -1.6 $V_{Ag/AgCl}$ to -0.6 $V_{Ag/AgCl}$. This scan was designed to avoid passive film formation at cathodic potentials and prevent premature surface damage under anodic conditions. Tafel analysis was performed within ± 50 mV vs. E_{corr} to determine the corrosion parameters.

Half-cell galvanostatic stripping measurements were conducted by initially holding the cell at OCP for 5 minutes, followed by stripping at current densities of 0.1, 0.25, 0.5, and 1 mA cm^{-2}. For the stripping-plating cycle, the three-electrode system remained the same, but the counter electrode was replaced from Pt to Zn to prevent electrolyte consumption due to side reactions at the Pt electrode. The cell was subjected to stripping and plating cycles by applying a current density of 1 mA cm^{-2} for 4 hours. The cutoff potential for stripping was -0.5 $V_{Ag/AgCl}$, and for the plating, it was -1.8 $V_{Ag/AgCl}$. Electrochemical impedance spectroscopy (EIS) measurements were performed in a three-electrode cell over a frequency range of 100 kHz-10 mHz. To evaluate changes during Zn plating, a constant current density of 1 mA cm^{-2} was applied for 5 or 60 minutes, by EIS at each time point.

The full-cell configuration consisted of freshly polished Zn discs as the anode and a porous carbon air-electrode (E4 type, ElectricFuel Ltd.) pressed onto a nickel mesh. The full-cell was constructed from three poly (methylmethacrylate) (PMMA) discs. The symmetrical exposed areas of the anode and air cathode in contact with the electrolyte were 0.44 cm^2. The cell was connected to a pump (RegloAnalogMs-4/112, Ismatec) and to a reservoir with capillary tube ($Ø_{in}$=0.75 mm, PEEK, BOLA). The electrolyte was circulated in bottom-top direction. Both ends of full-cell were connected to the same reservoir which contained 20 mL of the electrolyte. For discharge experiments, a continuous recirculation of the electrolyte from and to the reservoir was performed. The flow rate was adjusted to 1 mL min^{-1} for each cell. The schematic full-cell set up is shown in Figure S23. The electrolyte was circulated by pumping every 25 min for 5 min with a flow rate of 1 mL min^{-1} for each cell in order to provide enough dissolved Zn during cycling test. The intermittent operation of the pump was controlled by a TTL pulse via the analogue connection of the Biologic VMP3 potentiostat.

4.5. Quantitative calculation of desolvation energy barriers

The desolvation energy barriers (E_a) was calculated using Arrhenius equation [51]:

$$\frac{1}{R_{ct}} = Ae^{\frac{-E_a}{RT}} \quad (1)$$

Where R_{ct} is the interfacial resistance, A is the frequency factor, R is gas constant, and T is the absolute temperature.

4.6. Gravimetric weight loss method

The gravimetric weight loss of the Zn anodes was measured after 7 days of immersion in the electrolyte. After the experiment, the corrosion products were removed with saturated Gly or IDA solution according to ISO 8407 standard [52].

4.7. Material characterization

To investigate the formation of complex between Zn^{2+}-complexing agents, ultraviolet–visible (UV–vis) absorption spectra were obtained using a PerkinElmer Lambda 1050+ spectrometer in the 200–500 nm range. All measurements were conducted in quartz cuvettes to ensure UV transparency in the UV region. The reference solutions contained 2 M NaCl with 0.5 M Gly or 0.5 M IDA, and either 0.1 M or 0.01 M $ZnCl_2$, whereas the sample solution excluded $ZnCl_2$ to observe absorbance changes due to Zn^{2+} complexation. The $ZnCl_2$-contating electrolyte was used as the reference cell. Furthermore, Raman spectrum was obtained from KAISER Raman analyzer in range of 500-2000 cm^{-1}. After stripping or plating process, Zn anode was characterized using scanning electron microscopy (SEM, Quanta 650, FEI, USA) with the Everhart-Thornley Detector (ETD). SEM measurements were performed at an applied acceleration voltage of 20 kV. Elemental analysis was carried out using energy-dispersive X-ray spectroscopy (EDX) (Octane Super Detector, EDAX, USA), and the corresponding phase maps were obtained using TEAM EDAX software. Crystallographic characterization of the zinc anode was performed using X-ray diffraction (XRD) (Cu-source Empyrean, Malvern Panalytical, Germany). XRD pattern analysis was performed using HighScore software. Laser scanning microscopy (LSM) was performed using the OLYMPUS 3D laser microscope LEXT OLS 4000. Inductively coupled plasma optical emission spectrometry (ICP-OES) was conducted using the ZEA-3 system (Forschungszentrum Jülich) with a Thermo Fisher Scientific iCAP600 spectrometer, featuring an Echelle-optic and CID-semiconductor detector.

4.8. XCT measurement

The symmetric cell used for in operando X-ray computed tomography (XCT) imaging was designed in house and 3D-printed using photopolymer resin. A cross-section view of the cell is depicted in Figure S24. The design includes threaded openings at the top and bottom, that match the threads of commercial pipe fittings (G ¼'' BSP) used to secure the electrodes in place. Through the hourglass shape, it provides a region of interest (ROI), in which the material and the electrolyte volume are kept minimal, allowing for shorter exposure and therefore

improved temporal resolution of the in operando XCT imaging.

The electrode material was zinc wire (Ø = 0.5 mm, Thermo Scientific), which was mechanically cut to the desired length. The two-electrode system was constructed of two wire electrodes facing each other at a distance of around 2.5 mm. The tips of the wires were exposed to the electrolyte at a length of around 3.5 cm. For each cycling experiment, a current density of 1.0 mA cm^{-2} was applied. Plating and stripping steps were held for 4 h with a 3 h long OCV in between. We developed the 2D/3D imaging protocol based on Dzieciol et al. [53] Biologic SP300 potentiostat was used to control the electrochemical experiments in combination with a custom Python script reading the applied current from the potentiostat and triggering 3D scans during the OCV phases. All CT-measurements were conducted using a ZEISS XRADIA Versa 620 scanner. Prior to the operando protocol, a tomogram of the electrode's pristine state was collected. During each plating and stripping step, high-resolution 2D radiograms were acquired at an interval of 5 min to capture the development of the surface topology over time. At the end of each experiment, an additional tomogram was recorded depicting the post-mortem state of the electrode. For both, the 2D- and 3D-scans, the X-ray energy was kept at 20 kV with a low-pass filter to allow penetration of the housing material and the electrolyte volume, while maintaining sufficient photon counts for the metallic electrodes. Using a 20x objective, the voxel size of each scan of 1600 projections was around 0.7 – 0.9 μm with an exposure time of 5 s. The exact parameters for each experiment can be found in Table S4.

4.9. DFT simulation

Density Functional Theory (DFT) calculations for molecular binding energy calculations, structural optimization were conducted using Gaussian09 package with the level of B3LYP/6-311++G(d, p) basis set [54,55]. To describe water solvent environment, an implicit solvent model was adopted for all calculations with the dielectric constant value of 78. For each optimized structures of the solvent with Zn^{2+} ion, the binding energies (E_b) of the Zn^{2+} and solvent were calculated as $E_b = E(Zn^{2+}\text{-solvents}) - E(\text{solvents}) - E(Zn^{2+})$ with the basis set superposition error corrected by the counterpoise method.

To obtain binding energies between solvent and Zn surface, spin-polarized DFT calculations were performed by using Vienna ab-initio simulation package (VASP) code [56]. The plane wave energy cutoff 400 eV was adopted with PBE parameterization of GGA exchange-correlation functional [57]. We constructed a 4-layered slab for Zn(001) surface with 6×6 hexagonal unit cell whose lattice constant is 2.66 Å, and we inserted sufficient vacuum region greater than 15 Å to minimize unphysical interaction between periodic images. All structures were optimized in 2×2×1 k-mesh by fixing bottom 2 layers until all the atomic forces are less than 0.01 eV/ Å with the van der Waals correction by Grimme's D3 scheme [58]. The binding energies (E_b) were calculated by the equation, $E_b = E_{total} - E_{slab} - E_{solvent}$, where E_{total}, E_{slab}, and $E_{solvent}$ represent the total energy of slab with solvent, slab, and solvent molecule, respectively.

CRediT authorship contribution statement

Eunmi Im: Writing – review & editing, Writing – original draft, Investigation, Formal analysis. **Rebecca Erkes:** Investigation, Formal analysis. **Marie Heidler:** Investigation, Formal analysis. **Jinhong Mun:** Investigation, Formal analysis. **Saul Said Montiel Guerrero:** Formal analysis, Conceptualization. **Jee Ho Ha:** Formal analysis. **Krzysztof Dzieciol:** Investigation, Formal analysis. **Shicheng Yu:** Formal analysis. **Hans Kungl:** Writing – review & editing, Supervision. **Hermann Tempel:** Writing – review & editing, Supervision. **Geunsik Lee:** Supervision. **Yasin Emre Durmus:** Writing – review & editing, Supervision, Conceptualization. **Rüdiger-A. Eichel:** Supervision, Project administration, Funding acquisition.

Declaration of competing interest

The authors declare that they have no known competing financial interests or personal relationships that could have appeared to influence the work reported in this paper.

Acknowledgements

The researchers from IET-1, Forschungszentrum Jülich acknowledge the projects Verbundvorhaben iNEW2.0 (03SF0627A) and FeEnCap (13XP0536B) that were funded by the German Federal Ministry of Education and Research (BMBF).

Supplementary materials

Supplementary material associated with this article can be found, in the online version, at doi:10.1016/j.ensm.2025.104862.

Data availability

Data will be made available on request.

References

[1] Z. Zhu, T. Jiang, M. Ali, Y. Meng, Y. Jin, Y. Cui, W. Chen, Rechargeable batteries for grid scale energy storage, Chem. Rev. 122 (2022) 16610–16751, https://doi.org/10.1021/acs.chemrev.2c00289.
[2] Y.E. Durmus, H. Zhang, F. Baakes, G. Desmaizieres, H. Hayun, L. Yang, M. Kolek, V. Küpers, J. Janek, D. Mandler, S. Passerini, Y. Ein-Eli, Side by side battery technologies with lithium-ion based batteries, Adv. Energy Mater. 10 (2020) 2000089, https://doi.org/10.1002/aenm.202000089.
[3] P. Gu, M. Zheng, Q. Zhao, X. Xiao, H. Xue, H. Pang, Rechargeable zinc–air batteries: a promising way to green energy, J. Mater. Chem. A 5 (2017) 7651–7666, https://doi.org/10.1039/C7TA01693J.
[4] W.-F. Wu, X. Yan, Y. Zhan, Recent progress of electrolytes and electrocatalysts in neutral aqueous zinc-air batteries, Chem. Eng. J. 451 (2023) 138608, https://doi.org/10.1016/j.cej.2022.138608.
[5] Y. Li, H. Dai, Recent advances in zinc–air batteries, Chem. Soc. Rev. 43 (2014) 5257–5275, https://doi.org/10.1039/C4CS00015C.
[6] H. Wang, K. Wang, B. Liang, M. Wei, J. Xiong, D. Zhong, P. Pei, Solvation modification and interfacial chemistry regulation via amphoteric amino acids for Long-cycle zinc batteries, Adv. Energy Mater. 14 (2024) 2402123, https://doi.org/10.1002/aenm.202402123.
[7] H. Li, S. Guo, H. Zhou, Recent advances in manipulating strategy of aqueous electrolytes for Zn anode stabilization, Energy Storage Mater. 56 (2023) 227–257, https://doi.org/10.1016/j.ensm.2023.01.027.
[8] Q. Meng, T. Yan, Y. Wang, X. Lu, H. Zhou, S. Dong, Critical design strategy of electrolyte engineering toward aqueous zinc-ion battery, Chem. Eng. J. (2024) 154541, https://doi.org/10.1016/j.cej.2024.154541.
[9] R.B. Huang, M.Y. Wang, J.F. Xiong, H. Zhang, J.H. Tian, J.F. Li, Anode optimization strategies for zinc–air batteries, eScience (2024) 100309, https://doi.org/10.1016/j.esci.2024.100309.
[10] J. Wang, Y. Yang, Y. Zhang, Y. Li, R. Sun, Z. Wang, H. Wang, Strategies towards the challenges of zinc metal anode in rechargeable aqueous zinc ion batteries, Energy Storage Mater. 35 (2021) 19–46, https://doi.org/10.1016/j.ensm.2020.10.027.
[11] J.F. Parker, I.R. Pala, C.N. Chervin, J.W. Long, D.R. Rolison, Minimizing shape change at Zn sponge anodes in rechargeable Ni–Zn cells: impact of electrolyte formulation, J. Electrochem. Soc. 163 (2015) A351, https://doi.org/10.1149/2.1001602jes.
[12] C. Wang, J. Li, Z. Zhou, Y. Pan, Z. Yu, Z. Pei, S. Zhao, L. Wei, Y. Chen, Rechargeable zinc-air batteries with neutral electrolytes: Recent advances, challenges, and prospects, EnergyChem 3 (2021) 100055, https://doi.org/10.1016/j.enchem.2021.100055.
[13] F.T. Goh, Z. Liu, T.A. Hor, J. Zhang, X. Ge, Y. Zong, A. Yu, W. Khoo, A near-neutral chloride electrolyte for electrically rechargeable zinc-air batteries, J. Electrochem. Soc. 161 (2014) A2080, https://doi.org/10.1149/2.0311414jes.
[14] A. Sumboja, X. Ge, G. Zheng, F.T. Goh, T.A. Hor, Y. Zong, Z. Liu, Durable rechargeable zinc-air batteries with neutral electrolyte and manganese oxide catalyst, J. Power Sources 332 (2016) 330–336, https://doi.org/10.1016/j.jpowsour.2016.09.142.
[15] S. Clark, A. Latz, B. Horstmann, Rational development of neutral aqueous electrolytes for zinc–air batteries, ChemSusChem 10 (2017) 4735–4747, https://doi.org/10.1002/cssc.201701468.
[16] Y.E. Durmus, S.S. Montiel Guerrero, H. Tempel, F. Hausen, H. Kungl, R.-A. Eichel, Influence of Al alloying on the electrochemical behavior of Zn electrodes for Zn–Air batteries with neutral sodium chloride electrolyte, Front. Chem. 7 (2019) 800, https://doi.org/10.3389/fchem.2019.00800.
[17] S.S. Montiel Guerrero, Y.E. Durmus, K. Dzieciol, S. Basak, H. Tempel, S. van Waasen, H. Kungl, R.A. Eichel, Improved electrochemical performance of zinc

anodes by EDTA in near-neutral zinc− air batteries, Batteries Supercaps 4 (2021) 1830–1842, https://doi.org/10.1002/batt.202100332.
[18] W. Wei, J. Xu, W. Chen, L. Mi, J. Zhang, A review of sodium chloride-based electrolytes and materials for electrochemical energy technology, J. Mater. Chem. A 10 (2022) 2637–2671, https://doi.org/10.1039/D1TA09371A.
[19] W. Zhou, M. Yang, M. Chen, G. Zhang, X. Han, J. Chen, D. Ma, P. Zhang, Ion-sieving effect enabled by sulfonation of cellulose separator realizing dendrite-free Zn deposition, Adv. Funct. Mater. 34 (2024) 2315444, https://doi.org/10.1002/adfm.202315444.
[20] M. Li, Z. Li, X. Wang, J. Meng, X. Liu, B. Wu, C. Han, L. Mai, Comprehensive understanding of the roles of water molecules in aqueous Zn-ion batteries: from electrolytes to electrode materials, Energy Environ. Sci. 14 (2021) 3796–3839, https://doi.org/10.1039/D1EE00030F.
[21] L. Cao, D. Li, E. Hu, J. Xu, T. Deng, L. Ma, Y. Wang, X.-Q. Yang, C. Wang, Solvation structure design for aqueous Zn metal batteries, J. Am. Chem. Soc. 142 (2020) 21404–21409, https://doi.org/10.1021/jacs.0c09794.
[22] F. Yang, J.A. Yuwono, J. Hao, J. Long, L. Yuan, Y. Wang, S. Liu, Y. Fan, S. Zhao, K. Davey, Understanding H2 evolution electrochemistry to minimize solvated water impact on Zinc-anode performance, Adv. Mater. 34 (2022) 2206754, https://doi.org/10.1002/adma.202206754.
[23] R. Meng, H. Li, Z. Lu, C. Zhang, Z. Wang, Y. Liu, W. Wang, G. Ling, F. Kang, Q. H. Yang, Tuning Zn-ion solvation chemistry with chelating ligands toward stable aqueous Zn anodes, Adv. Mater. 34 (2022) 2200677, https://doi.org/10.1002/adma.202200677.
[24] A.R. Mainar, L.C. Colmenares, J.A. Blázquez, I. Urdampilleta, A brief overview of secondary zinc anode development: The key of improving zinc-based energy storage systems, J. Energy Res. 42 (2018) 903–918, https://doi.org/10.1002/er.3822.
[25] G. Juhel, B. Beden, C. Lamy, J. Leger, R. Vignaud, Effect of the surfactant "forafac" on hydrogen evolution on a zinc electrode, Electrochim. Acta 35 (1990) 479–481, https://doi.org/10.1016/0013-4686(90)87032-W.
[26] Y. Zhang, X. Fu, Y. Ding, Y. Liu, Y. Zhao, S. Jiao, Electrolyte solvation chemistry for stabilizing the Zn anode via functionalized organic agents, Small 20 (2024) 2311407, https://doi.org/10.1002/smll.202311407.
[27] S. Guo, L. Qin, T. Zhang, M. Zhou, J. Zhou, G. Fang, S. Liang, Fundamentals and perspectives of electrolyte additives for aqueous zinc-ion batteries, Energy Storage Mater 34 (2021) 545–562, https://doi.org/10.1016/j.ensm.2020.10.019.
[28] J. Cao, F. Zhao, W. Guan, X. Yang, Q. Zhao, L. Gao, X. Ren, G. Wu, A. Liu, Additives for aqueous zinc-ion batteries: recent progress, mechanism analysis, and future perspectives, Small 20 (2024) 2400221, https://doi.org/10.1002/smll.202400221.
[29] L. Zhang, M. Lin, Z. Yu, Y. Huang, Q. Sun, X. Lu, H. Cheng, Tyrosine additives with rich-polar functional groups provide multi-protections for ultra-stable zinc metal anodes, Energy Storage Mater. 75 (2025) 104022, https://doi.org/10.1016/j.ensm.2025.104022.
[30] Z. Luo, Y. Xia, S. Chen, X. Wu, R. Zeng, X. Zhang, H. Pan, M. Yan, T. Shi, K. Tao, B. B. Xu, Y. Jiang, Synergistic "anchor-capture" enabled by amino and carboxyl for constructing robust interface of Zn anode, Nano-Micro Lett. 15 (2023) 205, https://doi.org/10.1007/s40820-023-01171-w.
[31] B. Niu, C. Zhu, H. Yuan, W. Xu, Y. Liang, Z. Li, H. Jiang, Z. Cui, Z. Gao, S. Zhu, Organic molecular amino acids additives containing amide groups for uniform zinc deposition in aqueous zinc ion batteries, Small 21 (2025) e2409556, https://doi.org/10.1002/smll.202409556.
[32] S. Chen, D. Ji, Q. Chen, J. Ma, S. Hou, J. Zhang, Coordination modulation of hydrated zinc ions to enhance redox reversibility of zinc batteries, Nat. Commun. 14 (2023) 3526, https://doi.org/10.1038/s41467-023-39237-3.
[33] W. Deng, G. Li, X. Wang, Zinc-ion battery chemistries enabled by regulating electrolyte solvation structure, Adv. Funct. Mater. 34 (2024) 2405012, https://doi.org/10.1002/adfm.202405012.
[34] W. Zhou, T. Wu, M. Chen, Q. Tian, X. Han, X. Xu, J. Chen, Wood-based electrodes enabling stable, anti-freezing, and flexible aqueous zinc-ion batteries, Energy Storage Mater. 51 (2022) 286–293, https://doi.org/10.1016/j.ensm.2022.06.056.
[35] C. Lin, L. He, P. Xiong, H. Lin, W. Lai, X. Yang, F. Xiao, X.-L. Sun, Q. Qian, S. Liu, Adaptive ionization-induced tunable electric double layer for practical Zn metal batteries over wide pH and temperature ranges, ACS Nano 17 (2023) 23181–23193, https://doi.org/10.1021/acsnano.3c09774.
[36] E. Glycine., https://echa.europa.eu/de/registration-dossier/-/registered-dossier/14889/4/22.
[37] P.I. acid. https://pubchem.ncbi.nlm.nih.gov/, 2022.
[38] L. Côrte-Real, V. Pósa, M. Martins, R. Colucas, N.V. May, X. Fontrodona, I. Romero, F. Mendes, C.Pinto Reis, M.M. Gaspar, Cu (II) and Zn (II) complexes of new 8-hydroxyquinoline Schiff bases: Investigating their structure, solution speciation, and anticancer potential, Inorg. Chem. 62 (2023) 11466–11486. https://pubs.acs.org/doi/10.1021/acs.inorgchem.3c01066.
[39] A. Karim, M. Jan, R.E. Malekshah, N. Ullah, N. Ali, A. Haider, M. Iqbal, S. Ali, S. C. Hsu, M.N. Tahir, Structural and spectroscopic characterization of Zn (II) complexes: A computational perspective on anticorrosion potential of bronze surface, Inorg. Chim. Acta (2025) 122731, https://doi.org/10.1016/j.poly.2013.06.015.
[40] S. Rolfe, M. Patel, I. Gilmour, K. Olsson-Francis, T. Ringrose, Defining multiple characteristic Raman bands of α-amino acids as biomarkers for planetary missions using a statistical method, Orig. life Evol. Biosph. 46 (2016) 323–346, https://doi.org/10.1007/s11084-015-9477-7.
[41] H.G.M. Edwards, Spectra–Structure Correlations in Raman Spectroscopy. Handbook of Vibrational Spectroscopy, 2001.
[42] X.G. Zhang, Corrosion and Electrochemistry of Zinc, Springer, US, 1996.
[43] L. Baugh, Corrosion and polarization characteristics of zinc in neutral—acid media—I. Pure zinc in solutions of various sodium salts, Electrochim. Acta 24 (1979) 657–667, https://doi.org/10.1016/0013-4686(79)87048-6.
[44] M. Prestat, J. Soares Costa, B. Lescop, S. Rioual, L. Holzer, D. Thierry, Cathodic corrosion of zinc under potentiostatic conditions in NaCl solutions, ChemElectroChem 5 (2018) 1203–1211, https://doi.org/10.1002/celc.201701325.
[45] M. Remko, B.M. Rode, Effect of metal ions (Li^+, Na^+, K^+, Mg^{2+}, Ca^{2+}, Ni^{2+}, Cu^{2+}, and Zn^{2+}) and water coordination on the structure of glycine and zwitterionic glycine, J. Phys. Chem. A 110 (2006) 1960–1967, https://doi.org/10.1021/jp054119b.
[46] J. Mahler, I. Persson, A study of the hydration of the alkali metal ions in aqueous solution, Inorg. Chem. 51 (2012) 425–438. https://pubs.acs.org/doi/10.1021/ic2018693.
[47] S. Clark, A. Latz, B. Horstmann, Rational development of neutral aqueous electrolytes for zinc–air batteries, ChemSusChem 10 (2017) 4735–4747, https://doi.org/10.1002/cssc.201701468.
[48] L.-B. Ni, R.-H. Zhang, Q.-X. Liu, W.-S. Xia, H. Wang, Z.-H. Zhou, pH-and mol-ratio dependent formation of zinc (II) coordination polymers with iminodiacetic acid: Synthesis, spectroscopic, crystal structure and thermal studies, J. Solid State Chem. 182 (2009) 2698–2706, https://doi.org/10.1016/j.jssc.2009.06.042.
[49] Z. Hu, F. Zhang, A. Zhou, X. Hu, Q. Yan, Y. Liu, F. Arshad, Z. Li, R. Chen, F. Wu, Highly reversible Zn metal anodes enabled by increased nucleation overpotential, NanoMicro Lett. 15 (2023) 171, https://doi.org/10.1007/s40820-023-01136-z.
[50] Z. Guo, X. Mo, Y. Xu, X. Xu, L. Shi, H. Wan, L. Sun, W. Zhuang, M. Song, Glycine as a Bi-functional Electrolyte Additive for Favorable Zn Deposition, J. Electron. Mater. 53 (2024) 6594–6604, https://doi.org/10.1007/s11664-024-11397-y.
[51] X. Xu, X. Feng, M. Li, J. Yin, F. Li, J. Chen, W. Shi, Y. Cheng, J. Wang, Tailoring the solvation shells of dual metal ions for high-performance aqueous zinc ion batteries, Chem. Eng. J. 478 (2023) 147313, https://doi.org/10.1016/j.cej.2023.147313.
[52] A. DIN EN 8407:2021-04. Corrosion of metals and alloys - Removal of corrosion products from corrosion test specimens.
[53] K. Dzięcioł, Y.E. Durmus, H. Tempel, H. Kungl, A. Bauer, R.-A. Eichel, Laboratory X-ray computed tomography imaging protocol allowing the operando investigation of electrode material evolution in various environments, Iscience 26 (2023), https://doi.org/10.1016/j.isci.2023.107097.
[54] M. Frisch, G. Trucks, H. Schlegel, G. Scuseria, M. Robb, J. Cheeseman, G. Scalmani, V. Barone, B. Mennucci, G. Petersson, Uranyl extraction by N, N-dialkylamide ligands studied by static and dynamic DFT simulations, Gaussian (2009) 227, https://doi.org/10.1039/C4DT02443E, 09 9.
[55] A.D. Becke, Density-functional thermochemistry. III. The role of exact exchange, J. Chem. Phys. 98 (1993) 5648–5652, https://doi.org/10.1063/1.464913.
[56] G. Kresse, J. Furthmüller, Efficiency of ab-initio total energy calculations for metals and semiconductors using a plane-wave basis set, Comput. Mater. Sci. 6 (1996) 15–50, https://doi.org/10.1016/0927-0256(96)00008-0.
[57] J.P. Perdew, K. Burke, M. Ernzerhof, Generalized gradient approximation made simple, Phys. Rev. Lett. 77 (1996) 3865. https://journals.aps.org/prl/abstract/10.1103/PhysRevLett.77.3865.
[58] T. Bučko, S. Lebègue, J. Hafner, J.G. Angyan, Tkatchenko-Scheffler van der Waals correction method with and without self-consistent screening applied to solids, Phys. Rev. B 87 (2013) 064110, https://doi.org/10.1103/PhysRevB.87.064110.